Surfaces and Interfaces 82 (2026) 108466

Contents lists available at ScienceDirect

Surfaces and Interfaces

journal homepage: www.sciencedirect.com/journal/surfaces-and-interfaces

Long-term iron-bentonite interaction in a water-saturated room-temperature environment: Advancing for safety of metal waste containment in the geosphere

María J. Turrero [a,*], Elena Torres [a], Pedro L. Martín [a], Raúl Fernandez [b], Ana I. Ruiz [b], Almudena Ortega [b], Antonio Garralón [a], Belén Notario [c], Carlos Mota [b], Jaime F. Cuevas [b]

[a] Centro de Investigaciones Energéticas, Medioambientales y Tecnológicas (Ciemat), Avenida Complutense, 40, 28040 Madrid, Spain
[b] Universidad Autónoma de Madrid, Facultad de Ciencias, Calle Tomás y Valiente, 7, 28049 Madrid, Spain
[c] Centro Nacional de Investigación sobre la Evolución Humana (CENIEH), Paseo Sierra de Atapuerca, 3, 09002 Burgos, Spain

ARTICLE INFO

Keywords:
Radioactive waste containment
Long-term experiment
Fe corrosion
Bentonite
Microscale alteration
Fe mobility
Geological repository

ABSTRACT

Corrosion of C-steel containers may affect the long-term safety of deep geological repositories. To address uncertainties, the FeMo experiment was initiated in 2007 to evaluate iron mobility and bentonite alteration under aerobic conditions, granite-type water saturation, high corrosion rates, and room temperature. After 15 years, the experiment was dismantled for comprehensive analysis. The Fe-bentonite interface exhibited a multi-layered structure, with a black iron stripe and a brown-stained bentonite zone (2–5 mm thick). Altered iron comprised magnetite (50%), goethite (25%), siderite (5%), and ≈20% wt. metallic iron. The brown zone contained montmorillonite, cristobalite, feldspar, quartz, magnetite, goethite, lepidocrocite, and minor siderite. Chemical zonation of Fe, Mg, and Ca was observed within the first 0.5 mm from the interface. Iron penetrated up to 2–3 mm into the bentonite. Evidence of a trioctahedral clay component mixed with montmorillonite was found. Magnetite, carbonates, and Mg-rich clays precipitated under alkaline reducing conditions during the oxic-anoxic transient at the interface (<1 mm). This study's results are not only relevant for guaranteeing radioactive waste repository safety but also to assess other heavy metal containment strategies in other environmental applications, such as mines and landfills.

1. Introduction

Radioactive waste management is one of the biggest environmental challenges of this century. While short-medium-lived radioactive wastes are safely stored in surface-, or near-surface facilities, the storage of long-lived, high-level radioactive wastes (HLW) requires secure long-term management and still needs research. Deep geological repository (DGR) is currently the most widely accepted option for the management of HLW within the geosphere. The concept is inspired by nature, particularly uranium deposits. These deposits contribute to identifying the materials to be used in DGR and the processes that affect these materials' behavior in the storage system. It is primarily based on the use of multiple barriers to prevent the release of radionuclides into the environment (e.g. [1,2]). This multibarrier concept is also used for disposal and containment of other wastes, such as landfills, surface impounmendts, etc. [3,4].

In the context of HLW, the material chosen to isolate the waste from water until its temperature and radioactivity decrease is a metallic container made of copper or steel. Countries as Switzerland, France, Japan, Germany or Spain, among others, have chosen a carbon steel container (CSC) for waste encapsulation as the first barrier (summary in [5]). Compacted bentonite blocks or pellets are used as the sealing material between the CSC and the surrounding rock in the design of most HLW repositories, mainly because of its low permeability, swelling capacity, mechanical properties and sorption ability (review in [6]).

A critical aspect of DGR long-term safety is the geochemical interaction between the CSC and the bentonite barrier. Corrosion of the metal container and subsequent alteration of the bentonite could reduce the effectiveness of the repository's protective functions, potentially facilitating radionuclide migration. The corrosion process at the container surface is controlled by the thermo-hydraulic behavior of the clay barrier, determined by the heat generated from radioactive decay and the

* Corresponding author.
E-mail address: mj.turrero@ciemat.es (M.J. Turrero).

https://doi.org/10.1016/j.surfin.2026.108466
Received 29 July 2025; Received in revised form 17 December 2025; Accepted 9 January 2026
Available online 9 January 2026

ingress of groundwater through bentonite [5,7]. The resulting corrosion products may interact with bentonite, forming new iron-rich minerals that can influence important material properties such as swelling behavior and sorption capacity [8–11]. These processes may also influence the migration pathways of radionuclides by inducing chemical and physical changes at the interface (e.g. [12–14]).

Changes in environmental conditions, including saturation degree, temperature, redox state, pH, and the presence of dissolved species, affect the geochemical environment at the CSC-bentonite interface over the repository's lifespan. The types of corrosion products formed are governed by these evolving conditions, from initial operation through post-closure until equilibrium is reached. A detailed phenomenological description of the system and its evolution can be found in [5,15–16].

All corrosion reactions produce corrosion products, including insoluble hydroxides, carbonates, oxides, etc., which form microporous films on the metal surface, occupy more volume, and can facilitate the formation of pathways through which iron or iron-bearing radioactive contaminants can move [17–19]. In addition, corrosion products may interact with or migrate through bentonite, depending on factors such as [13,14,19,20]: (1) the microstructure and porosity of the bentonite; (2) the amount and chemical nature of the corrosion products; (3) the aforementioned environmental conditions (e.g., temperature, pH, or presence of other ions in the water); (4) iron uptake and adsorption on the surface of the clay particles, which would reduce transport. On the other hand, the evolution of the microstructure of the material depends on the degree of saturation and on the chemical evolution of the interface, which determines the potential exchange of chemical species.

The identification of corrosion products, the processes involved in their formation, the changes in the chemistry of the surrounding medium, the mobility and distribution, the impact they may have on the mobility of contaminants and their interaction with bentonite are essential to ensure the safety of the DGR. In this sense, the work presented here collects the results of the FeMo long-term experiment (15 years), which was designed to study the iron-bentonite interface in water saturated and room temperature conditions. The study aims to characterize modifications in solid phase composition from the micron to centimeter scale, changes in material microstructure and, in this context, the mobility of the iron corrosion products through the saturated-compacted FEBEX bentonite and the extension of the affected zone.

Analytical approaches involved two primary methods: (1) Description of microstructural patterns and physical features of the samples by X-ray microcomputed tomography (μ-CT) measurement. This non-destructive imaging technique is increasingly used in the study of materials, and in the specific case of bentonite, it has been used to analyze desiccation cracking processes [21], analysis of hydration process, water content and swelling [22,23], and microstructure [24,25]. It has also been used to analyze how particles move in soils ([26,27], and references therein). FeMo long-term experiment was analysed by μ-CT prior to destructive analyses to characterize porosity, pore connectivity, secondary features, iron movement and three-dimensional configuration at the sample scale (cm), which help to reduce uncertainties in the interpretation of analyses performed with other techniques; and (2) Analysis of corrosion products, alteration of montmorillonite, microstructure and iron penetration at the interface scale (μm-mm) by X-ray diffraction and scanning electron microscopy. The combined use of both approaches focused on improving existing understanding of the processes occurring at the iron-bentonite interface that may affect the repository's long-term safety.

2. Materials and methods

The FeMo long-term experiment is part of a broader investigation into the interaction between FEBEX bentonite and powdered iron, as described in [28]. This section draws on some of the material-related information presented in that study and expands upon it by providing a more detailed description of the experimental setup and the post-mortem analytical methods employed after dismantling.

2.1. FEBEX bentonite and iron powder

The materials selected for this experiment were compacted bentonite and iron powder. The bentonite was sourced from the Cortijo de Archidona deposit (Almería, Spain), identified by Enresa (the Spanish national radioactive waste management agency) as suitable for high-level radioactive waste (HLW) backfilling and sealing applications [29]. This clay was also employed in the FEBEX Project (Full-scale Engineered Barriers Experiment for a deep geological repository for high-level radioactive waste in crystalline host rock) to produce large-scale test blocks [29]. Throughout this study, this material is referred to as FEBEX bentonite.

FEBEX bentonite has been extensively characterized (e.g. [29]) and their main characteristics are summarized here. The montmorillonite content exceeds 90 wt. % (92 ± 3 %), with the smectite phase consisting of smectite-illite layers containing 10–15 % illite. The bentonite also contains variable amounts of quartz (2 ± 1 %), plagioclase (2 ± 1 %), trace K-feldspar, calcite and cristobalite-tridimite (2 ± 1 %). Its cation exchange capacity is 98 ± 2 meq/100 g, with exchangeable cations Ca (35 ± 3 meq/100 g), Mg (31 ± 3 meq/100 g), Na (27 ± 1 meq/100 g) and K (2.6 ± 0.4 meq/100 g). The clay's water content under laboratory conditions is approximately 13.7 ± 1.3 %.

Iron powder (Goodfellow, > 99 % purity) was used in contact with the bentonite. Powdered iron was selected over bulk carbon steel to enhance corrosion phenomena, particularly under the unsaturated and oxidizing conditions anticipated after repository closure. This conservative approach serves two purposes: first, to maximize the corrosion rate by increasing the specific surface area of iron particles and overcoming kinetic constraints; second, to lower O_2 fugacity by consuming residual oxygen during the corrosion process. Two iron powder fractions (60 μm and 450 μm) were used in the experiment.

2.2. Description of the test

The FeMo experiment was assembled in a 120 × 120 mm square container with a height of 16 mm, constructed from methacrylate and stainless steel 316 L (Fig. 1a, c). FEBEX bentonite was compacted to a dry density 1.6 g/cm^3 and placed into the cell at its hygroscopic water content (14 %). Six holes were drilled into the bentonite (see distribution in Fig. 1), and a porous sintered steel tube (0.45 μm pore size, 10 mm diameter and 2 mm wall thickness) was inserted into each hole. The gap between the sintered tube and the bentonite was filled with iron powder to a thickness of 2 mm, although slight variations may have occurred as a result of drilling irregularities. Three of the holes were filled with iron powder of 60 μm particle size and the other three with 450 μm iron powder (see Fig. 1d) to evaluate the effect of surface area on Fe mobility.

Hydration of the system was achieved through the sintered tubes using syringes equipped with O-rings (Fig. 1b, c). The syringes were filled with Ca-Na-HCO_3-type granitic water, representative of Grimsel Test Site water [30]. The experiment was conducted at room temperature, with laboratory temperatures ranging from 22 °C to 25 °C, over a 15-year period from May 2007 to September 2022. Photographs of the base of the experimental set-up, taken approximately five months after assembly (Fig. 1d) and on the day of dismantling 15 years later (Fig. 1e), reveal a uniformly saturated bentonite with no visible discontinuities and a brown halo (2–5 mm) distributed around the locations where metallic elements were inserted.

2.3. Dismantling and sampling

The experiment was dismantled inside a chamber maintained at low oxygen (sub-oxic) atmosphere (<1 % vol.). The sample was divided into

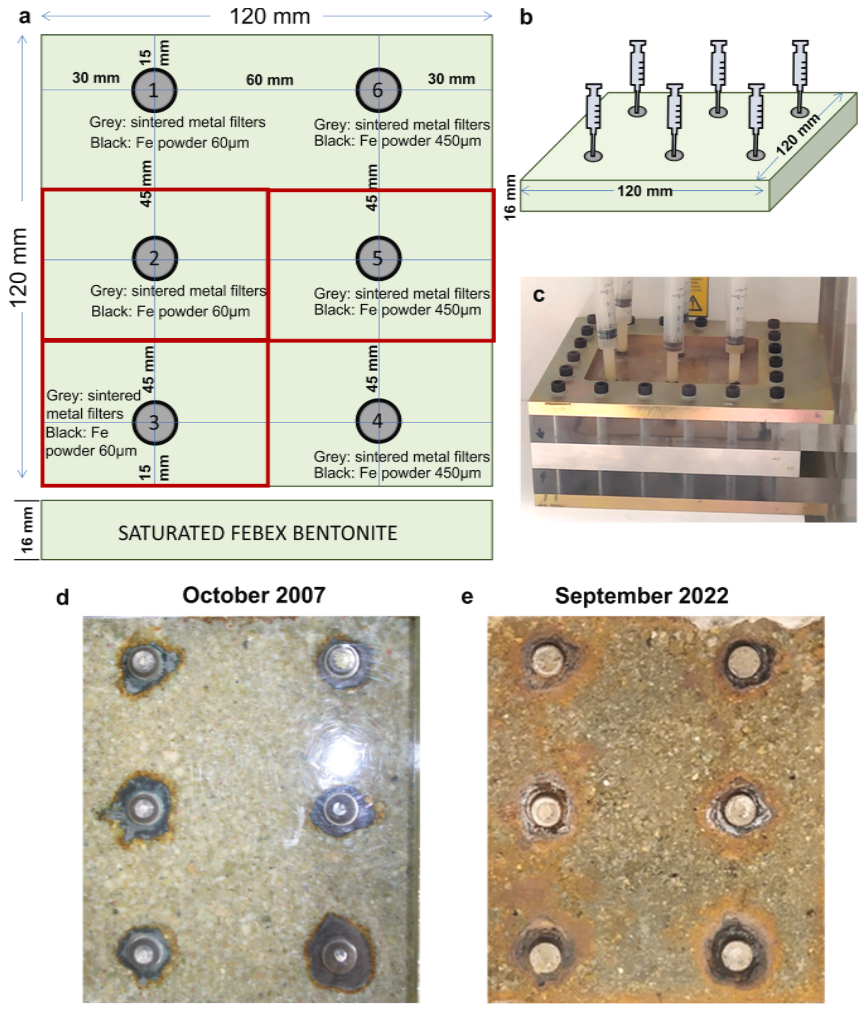

Fig. 1. a. Schematic diagram of FeMo experimental configuration. b. Schematic diagram of the FeMo cell and hydration system with syringes. c. Photograph of the experiment in its final configuration. It became operational in May 2007. d. Photograph of the base of the cell (the side opposite to the hydration) in October 2007. e. Photograph of the base of the cell taken during dismantling in September 2022. Photos d and e are oriented in the same way as the schematic in a, so that sections 1 through 6 correspond in the figure and photographs. The red rectangles correspond to the sections analysed in this work.

six sections, each containing bentonite, iron powder, and a sintered steel tube, along with its associated corrosion halo (Fig. 2). The maximum extent of the brown corrosion halo reaches 5 mm at the upper and lower flat contacts of the experimental setup (Fig. 2a-c), likely due to the presence of preferential pathways, for instance, at the interfaces between the material and the top or bottom lids of the cell, which are therefore considered artefacts. In contrast, the inner regions of the sample, which better reflect actual iron penetration (Fig. 2d), exhibit a maximum penetration depth ≈ 2 mm.

The visual appearance of the 6 sections was very similar. Sections 2 and 5 in Fig. 1a, both located in the central part of the experiment, with three of the sides in contact with other sections, were used to analyse the microstructure with X-ray microcomputed microtomography. Section 3 (Fig. 1a) was selected for the detailed mineralogical and microstructural analyses at the iron-bentonite interface.

The three sections were sealed with Araldite 2020 resin immediately after extraction in the anoxic glove chamber to protect them from contact with the atmosphere. Sections 2 and 5 were thus directly analysed by tomography. Section 3 was cut perpendicular to the iron powder ring and transversaly (Fig. 2c and d). For this, a Struers™ Secotom-6 cutter with a diamond blade was used, along with a water-free cutting fluid to prevent dehydration and avoid oxygen diffusion into the sample block. The sample was then immersed in hexane to remove the surface attached oil and frozen in liquid nitrogen. In this state, it was dehydrated under vacuum until reaching a pressure of $< 1{\cdot}10^{-6}$ Torr. The resulting dry surface was flat and homogeneous and used to create elemental distribution maps and profiles to detect concentration gradients in SEM-EDX observations. To complete the preparation, the samples were coated with gold using a Q150T-S Quorum sputter coater system.

2.4. Methods of analysis

X-ray microcomputed tomography (µ-CT) was employed as a non-destructive technique to generate two-dimensional cross-sections and reconstruct three-dimensional models, enabling detailed analysis of the microstructure in Sections 2 and 5. Imaging was conducted at the National Research Center of Human Evolution (CENIEH, Burgos, Spain) using a TESCAN CoreTOM MicroCT system with micron-scale spatial resolution. Differences in X-ray absorption between various materials and phases facilitated the identification of microstructural features from the resulting images. Pore size, orientation, and interconnectivity were characterized in collaboration with CENIEH, utilizing both Dragonfly ORS [31] and FIJI visualization and image analysis [32] software. CT technical parameters for each sample and the number of projections used for three-dimensional reconstruction and analysis are in Table 1.

The total cation exchange capacity (CEC) of the bentonite samples

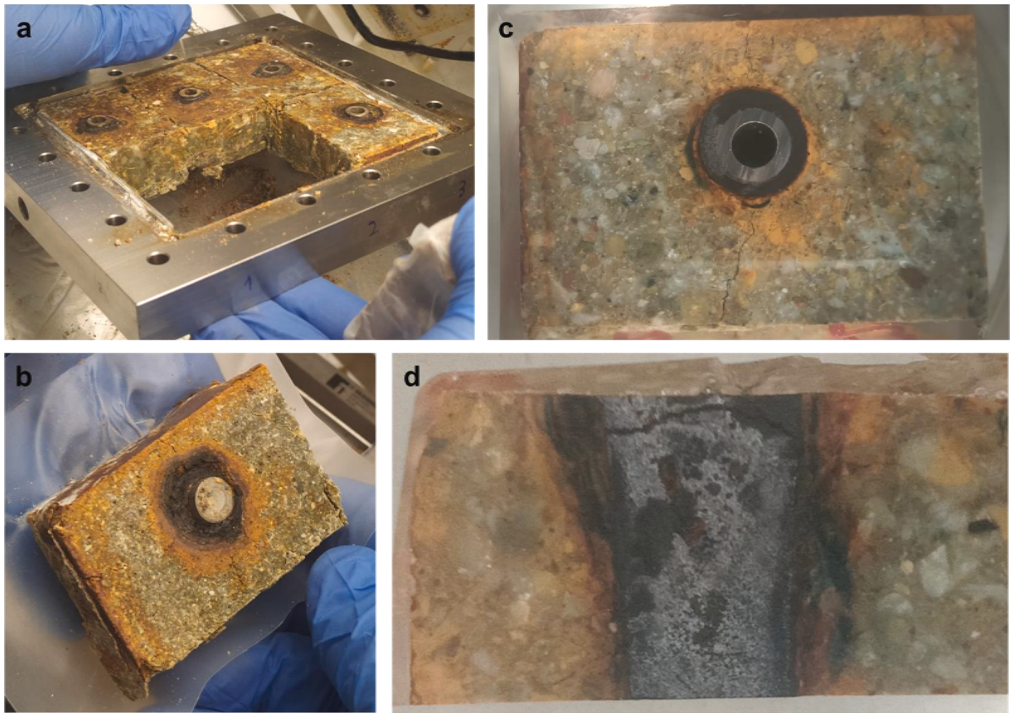

Fig. 2. a. Image of the FeMo test dismantling in a suboxic chamber, with the sample cut into six 40 × 60 mm sections. b. Detail of Section 3. c. Section 3 once cut for the analysis (see cut details in the text). d. Cross-section of Section 3.

Table 1
Micro-CT settings for Sections 2 and 5 of FeMo experiment.

	FeMo exp. Section 2	FeMo exp. Section 5
Focus mode	microfocus	microfocus
Accelerating voltage (kV)	180	180
Tube current (μA)	144	211
Tube power (W)	26	38
Total scan time (min)	133	95
Exposure time (s)	1.3	0.9
Total projections	2900	3000
Filter	1 mm Cu	1 mm Cu
Resolution	26 μm/voxel	38 μm/voxel

was determined according to the method described in [33]. This approach relies on replacing the native exchangeable cations in the clay with Cu^{2+} ions and then measuring the absorbance of electromagnetic radiation at 620 nm using a UV–visible spectrophotometer. The distribution of exchangeable cations was established using $CsNO_3$ as a displacing agent [34], and the concentrations of the major cations were quantified by ion chromatography (Dionex DX-4500i).

To extract adsorbed iron, a modified procedure based on [35] was employed, using 0.3 M citric acid as the extraction solution. This chelating agent targets the more reactive adsorption sites on the clay surface but does not dissolve amorphous Fe oxides or magnetite/ilmenite; neither structural Fe nor exchangeable Fe is affected. Accordingly, iron measured with this protocol is attributed primarily to Fe bound at reactive montmorillonite surface sites. Removal of free iron oxides from clay samples was achieved using the citrate-bicarbonate-dithionite protocol [36], which does not significantly alter iron silicate clay minerals or cation exchange capacity. Thus, iron concentrations obtained in this step are associated mainly with iron oxides, and no alteration of the bentonite matrix is expected. Total iron in bentonite at different distances from the interface was analysed by Bruker CTX 800 Portable Countertop XRF Analyzer.

All analyses were performed in duplicate, and unaltered FEBEX bentonite served as the reference material for comparison.

Mineralogical changes along the bentonite block and at the iron interface were studied by X-ray diffraction (XRD). Samples weighing approximately 1 g, and <0.5 g at the iron interface, were dried in a desiccator with silica gel to avoid atmospheric moisture uptake. The dried samples were ball-milled in a MM200 RETCH™ device with zircon vessels and balls, followed by final manual homogenization in an agate mortar to achieve mean grain sizes below 5 μm. Prior to XRD analysis, sample powders were equilibrated to 55 % relative humidity to standardize water content. Analyses were conducted using a Bruker D8 Discover diffractometer, equipped with a Johansson-type Ge 111 curved primary monochromator for Cu-Kα_1 radiation and a LYNXEYE XE-T high-resolution, energy-dispersive 1-D detector, which eliminates fluorescence and Kß radiation. The patterns were measured in a range of 3–70° θ/2θ, with angular increments of 0.02° and times of 1 s. The instrument operated at 40 kV and 40 mA. For the samples taken near to the interface (<1 mm from the heater), the iron powder and the bentonite, airtight sample holders were used. Phase identification in diffractograms was performed using X'Pert HighScore Plus® software (PANalitycal™), and phase quantification at the interface was achieved via the RIR semiquantitative method, which typically yields absolute errors of ±20 % [37]. The presence of high atomic number grains such as Fe (and thus higher X-ray absorption) may contribute less to the diffraction signal through the microabsorption effect, resulting in inaccurate intensity measurements. The errors due to this effect are small compared to those inherent in the RIR method used [38], although the values are sufficiently accurate for the identification and semiquantification approach pursued. The International Centre of Diffraction Data (ICDD) powder diffraction files (PDF) standards supported in High Score Expert Plus© software (version 2.1.b 2005) were used for mineral checking.

Surface morphology and imaging analyses were performed with a Hitachi S-3000 N scanning electron microscope (SEM) coupled with an EDX XFlash® 6130 Bruker detector, on thin layers (<5 mm) containing a transverse section of pressed iron powder (previously embedded in resin during the dismantling). To remove water from the iron-bentonite layers, samples were first immersed in liquid nitrogen for 30 min to freeze water, followed by vacuum drying at $<10^{-6}$ Torr for 2–3 days.

Dried samples were embedded in Araldite 2020™ resin for ease of handling and subsequent sectioning. The resulting pieces were polished with progressive sandpapers to obtain flat surfaces amenable to microscopic analysis, with specific attention to preserving the integrity of the iron-bentonite interface due to the expected narrow extent of alteration. Final preparation included gold coating using a Q150T-S Quorum sputter coater system.

3. Results and discussion

3.1. X-ray microcomputed tomography

X-ray microcomputed tomography was performed on Sections 2 and 5 of the FeMo experiment (Fig. 1). Fig. 3 shows three images of Section 2 and one image of Section 5, as an example of a 3D reconstruction and stacks. The lighter and brighter areas in the images corresponds to the sinter and the iron, while the rest is the bentonite, darker and less bright. Black should correspond to macropores and/or microcracks.

Fig. 3a is a slightly rotated 3D reconstruction of the Section 2 after processing the image to convert the color from grayscale to brownscale and enhance the contrast to better observe patterns and features of the sample. The image shows a massive and compact sample with some color (brownscale) variations indicating differences in density due to the presence of grains of different size and composition dispersed in the montmorillonite (matrix). The matrix makes up most of the sample and is homogeneous, indicating that the bentonite is saturated. Fig. 3b is a two-dimensional slice of a cross-section of Section 2 showing microcracks perpendicular to the sintered tube plus iron insertion hole, and also in the contact between iron and bentonite. None extend all the way throughout the bentonite, and sometimes they extend in favor of the grain boundaries. Fig. 3c is a two-dimensional projection of an apical view of Section 2 showing some microcracks in radial configuration with respect to the sintered tube plus iron insertion hole. The extent of the microcracks is limited, and most of them do not prolong >20 mm from the interface. There are no secondary microcracks in either image b or c, and no density changes are observed along the main radial and perpendicular microcracks, which are clean, and thus it is assumed that bentonite is saturated and microcracks are air-filled (black). Fig. 3d is a two-dimensional slice of a cross-section of Section 5 showing a close detail of the sinter-iron-bentonite interface, which has very sharp and nitid contacts.

Two-dimensional slices were used to quantitative analysis of porosity, pores connectivity and metal particles penetration. The analysis was performed after segmenting (i.e. isolate the region of interest) the features of interest (e.g. pores) in the images to obtain a three-dimensional network (skeleton) that provides the spatial distribution of each feature.

The total porosity was quantified as volume of pores of the section, which is calculated as the ratio of total volume of pores (skeleton of Sections 2 and 5 in Fig. 4a, b, respectively) to volume of the region of interest (*100). Pores (mean volume) were classified into two different volume intervals: as > 0.01 mm^3 or < 0.01 mm^3. Pore orientation was calculated from the *theta* (θ) and *phi* (ϕ) parameters. The value of *theta* (θ), ($-180° < \theta < 180°$), is the angle between the X axis and the projection of the longest axis of the pore on the X-Y plane. The value of *phi* (ϕ), ($0° < \phi < 90°$), is the angle between the Z axis and the longest axis of the pore.

Pore connectivity was calculated using two different methods: the

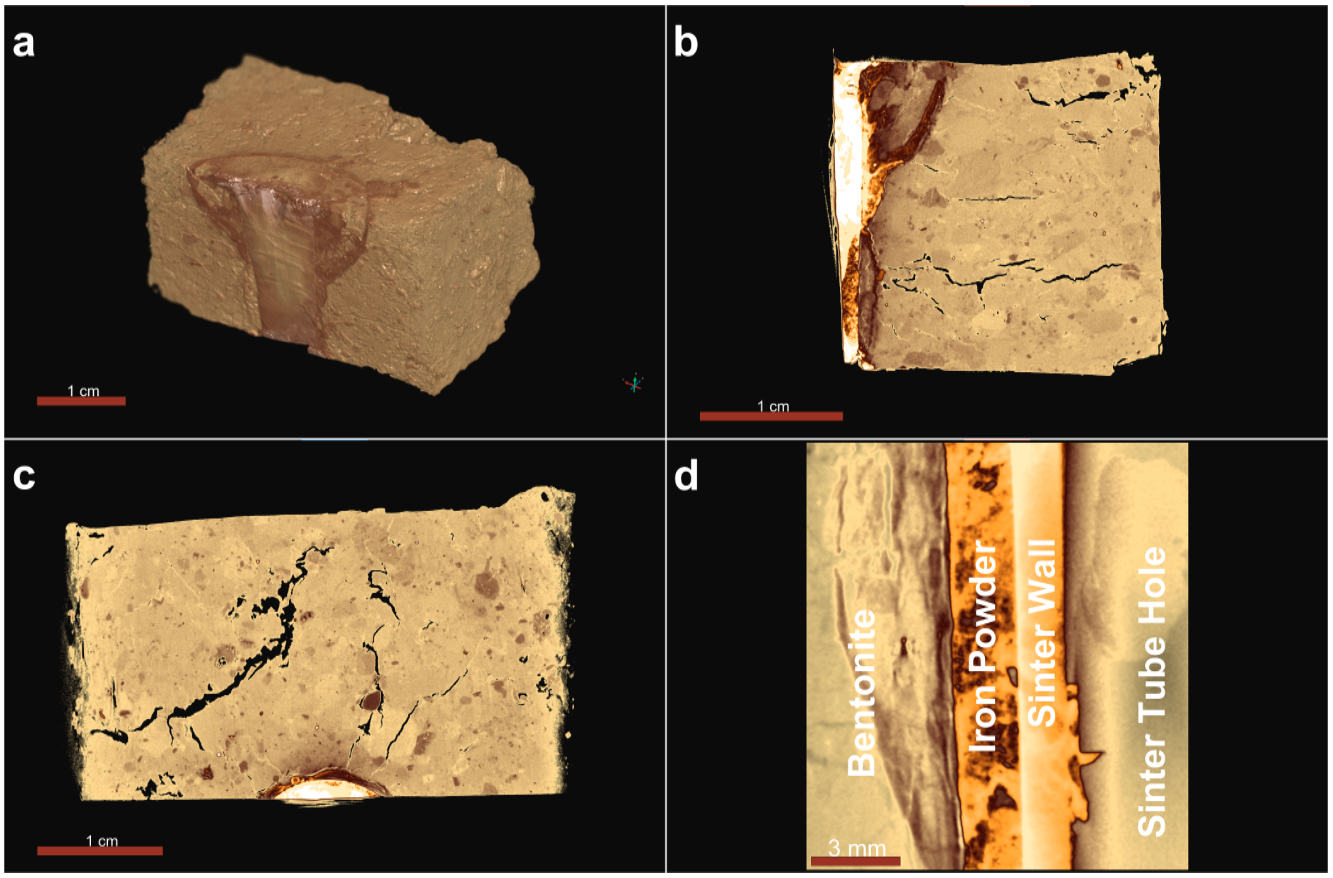

Fig. 3. Different images of FeMo experiment after 15 years (see Fig. 2 and Figure). a. 3D X-ray microcomputed tomography reconstruction of Section 2. b. 2D slice showing a slightly rotated cross-section of Section 2. c. 2D slice showing a part of the apical view of Section 2. d. Stack showing a close detail of the sinter-iron-bentonite interface of Section 5.

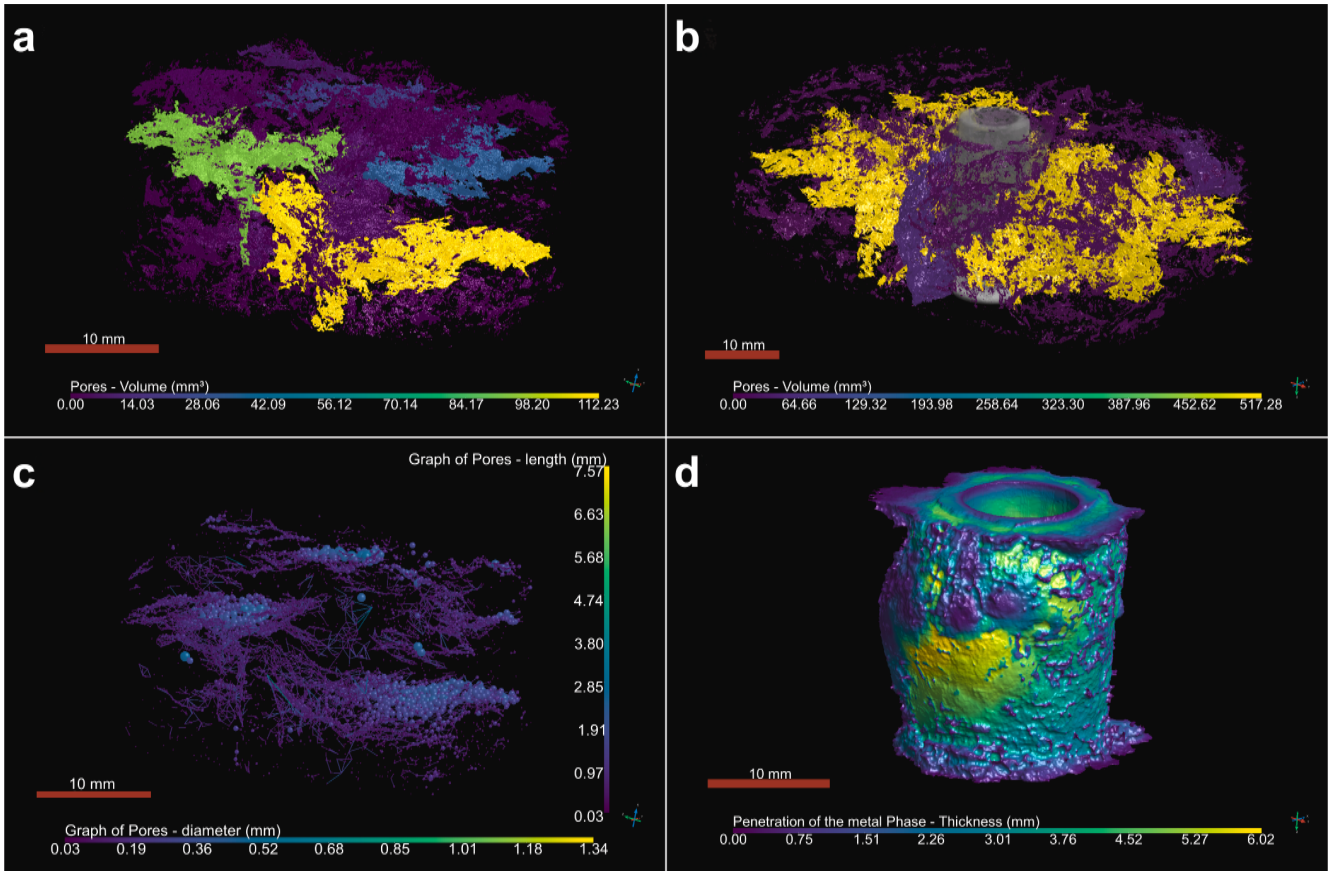

Fig. 4. 3D reconstruction of pore space of Section 2 (a) and Section 5 (b) and 3D reconstruction of pore connections of Section 5 (c) and iron penetration of Section 5 (d).

Pore Network Model (PNM), comprehensively detailed in [39], and the BoneJ plugins, part of the ImageJ software developed for bone image analysis, which is described in [40], with example of applicability to soils in [41]. The Pore Network Model gives results of relative frequency of diameter, related to nodes (pores), and length, understood as length of throats connecting nodes. The BoneJ provides results on connectivity in terms of number of trabeculae or branched structures forming a three-dimensional network (like those supporting bones), which is then translated into connectivity density (ConnD) or number of trabeculae per unit volume (cm^3) (e.g. skeleton of Section 5 in Fig. 4c).

The penetration of iron into the bentonite was calculated as the maximum width of the metallic particles from the inner wall of the sintered tube (e.g. skeleton of Section 5 in Fig. 4d). That is, the 2 mm thickness of the sintered pipe wall and the 2 mm thickness of the metallic iron must be subtracted from this maximum value to obtain the maximum penetration of the iron into the bentonite.

Results of each parameter for Sections 2 and 5 of the FeMo experiment are in Table 2. Due to the resolution of micro-CT, the pore size and volume identified are macropores, which represent a small portion of the total porosity and pore size distribution of bentonite [42], but which may be important for particle mobility. PNM analysis shows that the most common pore diameter is in the range of 50 to 100 μm, which corresponds to the intergranular pore space. As shown in Fig. 4, a complex network of macropores of variable size and continuity exists in the two sections analyzed, although the density of connections and extension (continuity of microcracks) is greater in Section 2 (312 cm^3) than in Section 5 (236 cm^3) (Table 2). In both cases there is approximately the same proportion of microcracks with an orientation perpendicular to the sintered tube plus the iron than radial to it. The maximum iron penetration in Section 2 is 4.49 mm, so by subtracting the 4 mm of sintered wall and iron, we have a maximum iron penetration thickness of 0.49 mm. In section 5, the maximum penetration of metallic particles is 6.02 mm, so by subtracting the 4 mm of sintered wall and iron, we would have a maximum iron penetration of 2.02 mm.

Table 2
Data of different physical parameter of Sections 2 and 5 of the FeMo experiment.

	FeMo – Section 2	FeMo – Section 5
Volume of pores	348.6 mm^3	841.9 mm^3
Porosity	2.2 % (→ 99.8 % of the pores are below 0.01 mm^3)	1.7 % (→ 99.5 % of the pores are below 0.01 mm^3)
Pore orientation	≈ 45 % of the pores are radial to the sinter and ≈ 55 % are perpendicular	≈ 65 % of the pores are radial to the sinter and ≈ 60 % are perpendicular
Connectivity	More and longer branches (compared to Section 5) ConnD = 311.6 cm^3	Less and shorter branches (compared to Section 2) ConnD = 235.9 cm^3
Metal particles penetration	0.49 mm	2.02 mm

The presence of microcracks and the differences between the two sections may be due to several reasons: (1) heterogeneity of the bentonite leads to microcracks appearing during the hydration process due to differential expansion. The cracks gradually close as the bentonite hydrates, but the rate of crack propagation is greater than the rate of closure [43], and if hydration is not complete, unsealed microcracks may remain; (2) microcracks formed during drilling to insert the sintered tube and iron which could reopen while dismantling operations; (3) the microcrack network may have been induced by the presence of gas by corrosion at some point in the early stages of the corrosion process [18,44], which could have caused irreversible heterogeneities if

resealing is avoided because uncomplete hydration, as mentioned above, or because of walls are coated with Fe(III) as observed by [19] in their experiments; the latter, in terms of dehydration, is unlikely, however, no density changes are observed inside the fractures in the different slices, which leads to believe that the centimeter-scale microcracks are filled with air; and (4) a combination of the above.

Variations in iron penetration values may result from sample heterogeneity (for example, in terms of volume of pores), fracture network geometry, or differences in iron powder particle size, which affect surface reactivity, oxidation kinetics, and aggregation tendencies, potentially influencing iron mobility (e.g., [45]).

3.2. Chemical gradients

Table 3 shows the results of chemical gradients in Section 3 of the FeMo experiment. The cation exchange capacity (CEC) of the bentonite remains unchanged except in the interface zone where the clay is affected by the presence of corrosion products and the CEC decreases. Some variations in the exchangeable cations are observed when compared to the data of the original FEBEX bentonite: Na decreases at the interface, Ca decreases slightly at 5–10 mm from the interface and increases at <5 mm from the interface; Mg increases at 5–10 mm from the interface and has values slightly higher than reference at <5 mm from the interface.

The highest iron concentrations are found in the first 2 mm from the interface. Amorphous iron (oxides) are present in high concentrations (208 mmol/100 g) in the first 5 mm near the interface. At 5 mm from the interface, the concentration decreases sharply, although the concentration is still higher than that measured in the reference FEBEX bentonite.

Table 3 also shows the proportions of Fe, Ca, Mg, Al and Si measured by XRF, and the data normalized to aluminum, as this is a relatively immobile element in bentonite. This makes possible to detect variations along a profile from the interface. It is observed that there is an increase of Ca and a slightly decrease of Mg at the interface. Fe is high in the first two millimeters from the interface, which agrees with the high concentration of amorphous iron, and the anomaly extends for the first 5 mm. Silicon remains more or less constant.

3.3. Mineralogy

The cylindrical section containing steel and compacted iron powder in contact with compacted bentonite is characterized by a black stripe (iron powder), followed by a brown zone of variable thickness (2–5 mm) that stains the bentonite a yellowish-green color. The black strip, corresponding to the iron powder in contact with the FEBEX bentonite in Section 3 of the FeMo experiment (Fig. 3c), was analysed by XRD under hermetically sealed conditions and was consistently protected from exposure to atmospheric oxygen. Semiquantitative data were obtained using the reference intensity ratio (RIR) method, as implemented in the X'Pert HighScore software (2005, Panalytical).

Fig. 5 shows the location of the samples used to determine the mineralogical composition of the altered iron powder and its contact with the bentonite. The main corrosion product of the iron powder is magnetite (Fe_3O_4 = 50 wt. %), accompanied by goethite (FeOOH = 25 wt. %) and minor amounts of siderite ($FeCO_3$ = 5 wt. %), while approximately 20 wt. % of metallic iron remains unaltered. The brown-stained bentonite at the contact zone contains, in addition to the typical bentonite minerals (montmorillonite, cristobalite, feldspars, and quartz), magnetite, and the iron oxyhydroxides goethite and lepidocrocite, with minor amounts of siderite. The bentonite near this contact retains the same composition as the original material described in Section 2.1.

The presence of both aerobic and anaerobic corrosion products indicates that a transition from oxic to anoxic conditions occurred, and the thermodynamical stability of magnetite, which is the prevailing Fe-mineral phase, requires alkaline (pH >8) and redox conditions. The presence of iron carbonate also supports this environment (i.e. [46–48]).

3.3.1. Microstructure at the interface

The stripe of powdered iron around the sintered steel cylinder is clearly visible in the longitudinal section photograph and in the SEM backscattered electron (BSE) images of the Fig. 6a. The BSE image shows a compact white stripe corresponding to the steel cylinder and a more porous light grey stripe that is the iron powder in contact with the bentonite. These zones correspond to the bright, black and ochre zones in the photograph. The contacts between the various components are very straight and well defined. The elemental map of Fe along the 2 cm segment marked in the photograph of the Fig. 6a shows that the halo of Fe diffusion reaches up to 1–2 mm into the bentonite. This halo is segmented in a zone of high Mg concentration, 0.1–0.3 mm, and a zone of high Ca concentration, 0.2–0.3 mm, measured from the interface with the iron powder (Fig. 6b). These anomalies are very restricted to the first 1.0 mm zone closest to the interface, except for iron, which penetrates up to 2–3 mm into the bentonite. This is consistent with the results of chemical gradients shown in Table 3 and the results of iron penetration measured from the micro-CT images for Sections 2 and 5.

Fig. 6c shows high-resolution quantitative elemental profiles measured in an area adjacent to the elemental mapping. The profiles correspond to the integrated EDX analysis of rectangular strips (0.5 mm wide) bounded every 100 μm for the first 3 mm and every 500 μm to the end of the bentonite from the interface with the iron powder. A strong increase in Fe content is observed from about 3 mm towards the interface. After 3 mm, the composition of the bentonite remains very constant, with occasional anomalies due to the presence of mineral fragments (quartz, feldspars) of larger size compared to the usual grain sizes of the bentonite minerals.

Fig. 6d shows the normalized elemental ratio with respect to Al, considering this element to be relatively immobile in the bentonite,

Table 3
Bentonite chemical gradients from the Section 3 of the FeMo experiment along a profile extending from the interface with the iron powder to 15 mm from the interface.

Distance to interface	CEC	Na	K	Mg	Ca	adsorbed-Fe	amorphous-Fe
		cmol(+)/Kg				mmol/100 g	
interface	90.8 ± 0.0	21.1	2.3	29.2	39.3	—	207.9
2 mm	98.8 ± 0.0						
5 mm	99.0 ± 0.0	27.9	2.9	33.8	34.2	1.9	48.3
10 mm	99.5 ± 0.2					4.1	35.7
FEBEX ref.	98.1 ± 0.1	25.6	3.1	28.9	37.2	0.9	1.0

Distance to interface	Fe %wt.(XRF)	MgO	Al_2O_3	SiO_2	Ca	Ca/Al	Mg/Al	Fe/Al	Si/Al
interface	13.74	1.48	5.30	21.65	0.78	0.28	0.32	4.90	3.61
2 mm	6.94	3.43	12.11	48.18	1.18	0.18	0.32	1.08	3.51
5 mm	3.28	4.48	13.73	55.47	1.05	0.14	0.37	0.45	3.57
10 mm	3.09	3.96	13.69	54.24	1.31	0.18	0.33	0.43	3.50
FEBEX ref.	2.34	4.41	13.73	55.27	1.10	0.15	0.37	0.32	3.56

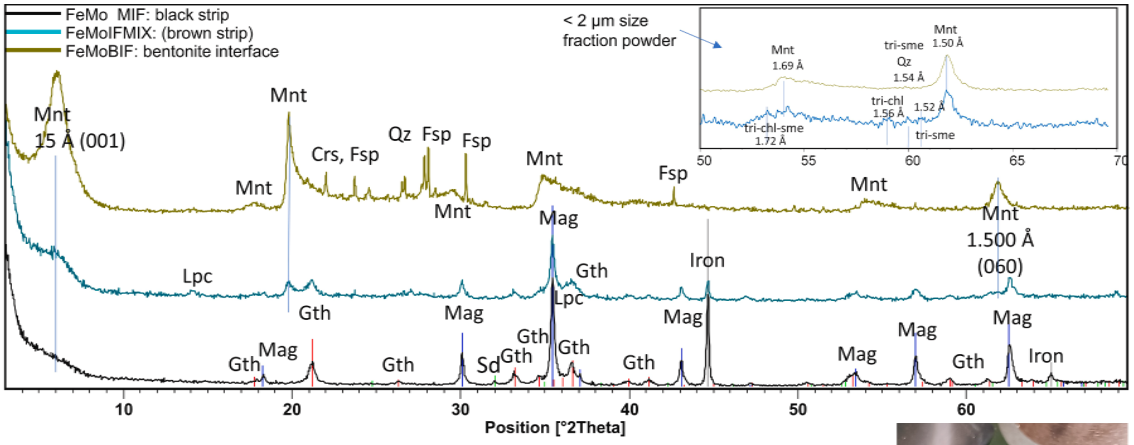

Mineralogy (%) Sample	Mnt	Qz,Crs,Fsp	Lpc	Gth	Mag	Sd	Iron
Iron powder (MIF)	<5	-	-	25	50	5	20
Iron interface (IFMIX)	40	<5	5	10	40	<5	<5
Bentonite interface (BIF)	90	10	-	-	<5	-	-

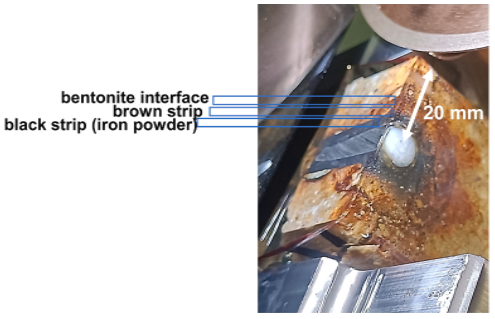

Fig. 5. Section 3 of the FeMo experiment. XRD powder patterns. Semiquantitative (% weight %) mineralogy of altered iron powder cylinder and bentonite interface. Mnt: montmorillonite; Qz: quartz; Fsp (feldspar group minerals); Crs: cristobalite; Lpc: lepidocrocite; Gth: goethite; Mag: magnetite; Sd: siderite; Iron: unaltered iron powder. XRD of < 2 µm size fraction powder, prepared punctually by dispersion and sedimentation, was added to show a detail of 50–70 °2θ region. Tri: tri-octahedral; Chl: chlorite; Qz: quartz; Sme: smectite.

which makes possible to highlight variations in Fe and any other element. As can be seen from the maps in Fig. 6b, from the elemental ratios there is a 2 mm thick zone of high Fe/Al ratio that progressively decreases to values of the reference bentonite about 3 mm from the iron-bentonite contact. A maximum in Ca/Al ratio is also observed just at the interface, and the K concentration in the first millimeter, whose distribution appeared dispersed in the plot of absolute contents in Fig. 6c, stands out.

Fig. 7a shows a section (BSE) of the powdered iron in which 4 layers can be distinguished. The layer in contact with the sintered tube, of about 1.1 mm, with bright white grains of about 40 µm of powdered iron. Next a layer of about 0.2–0.3 mm in which some shiny grains of metallic iron are still visible and a rather compact gray matrix corresponding to corrosion products. Then a very porous layer (pores are black in the image) of about 0.2–0.4 mm of corrosion products, suggesting that conditions have allowed the dissolution of iron in aqueous phase in this zone. The last layer, in contact with the bentonite, about 0.3 mm, has a low porosity and no metallic iron grains are observed, only the corrosion products, which may cover the iron grains and prevent them from being visible.

The fragments studied at the contact between the iron powder layer and the dark brown bentonite rim show a sharp transition between the iron oxide zone (altered iron powder) and the cemented bentonite edge (no cracks are observed within the first milimeter, as seen in the images in Fig. 6). Fig. 7(b, c) highlights the distinct contact of the oxide zone. Near this contact, the bentonite appears in layers, leaving sub-rounded voids, indicating that this area has been affected by fluid (liquid or gas) flows induced by water transport and chemical reaction (Fig. 7d). As in Fig. 6a, the elemental maps show the accumulation zones of Mg, Fe and Ca (Fig. 7e).The iron-rich material (oxide) exhibits a flat fracture and reveals voids corresponding to former Fe metal grains (Fig. 7c, f, g). This contact zone has been observed at higher magnification to further describe its texture and conduct chemical analyses.

The textures and compositions of the different zones of the interface have been studied in detail on fresh fractures fragmented under anoxic conditions. Fig. 8 shows the contact between the bentonite and the dark ochre-stained zone. The concentration of Fe is evident within the first 100 µm from the contact (Fig. 8a, b, c). Continuous staining is not observed within the first mm; instead, there are localized concentrations that appear to have spread through cracks (Fig. 8d). These localized concentrations also contain other crystals corresponding to potassium feldspar compositions and needle-like aggregates rich in calcium on plagioclase crystals.

A detailed view of a fresh fractured clay surface free of Fe staining is shown in Fig. 8e. Table 4 presents the chemical composition of these distinctive zones (in Fig. 8e), demonstrating the presence of potassium feldspar and plagioclase (FeMo 1 and 2), as well as mica-like mineral sheets of celadonitic composition (low tetrahedral charge; FeMo3). The clay aggregates (in Fig. 8f, FeMo4) are compact aggregates with perforated sectors that seem to contain pores. On average, their composition is rich in Fe and Mg compared to FEBEX montmorillonite [49], and the sum of octahedral cations is between a di-octahedral and tri-octahedral composition, which is consistent with the possible incorporation of Fe and Mg into the smectite phase.

XRD patterns in Fig. 5 show reflections compatible with the presence of trioctahedral phyllosilicates (chlorite and smectite; [50]) in the <2 µm fraction of the sample corresponding to the brown strip (1.72, 1.56, 1.52 Å in FeMo IFMIX sample). Given the coexistence of these reflections with those of dioctahedral smectite, this is consistent with the FeMo4 analysis in Table 4.

Fig. 9 contains chemical analyses (EDX) characteristic of the iron oxide–bentonite transition zone. The iron-rich zone (Fig. 9a) consists exclusively of Fe, O, and C. Insignificant amounts of $FeCO_3$ (siderite) have been detected through XRD. It should be noted that carbon analysis ($Z = 12$) has a high degree of error in this technique, and C also appears as environmental contamination from the conductive graphite adhesive

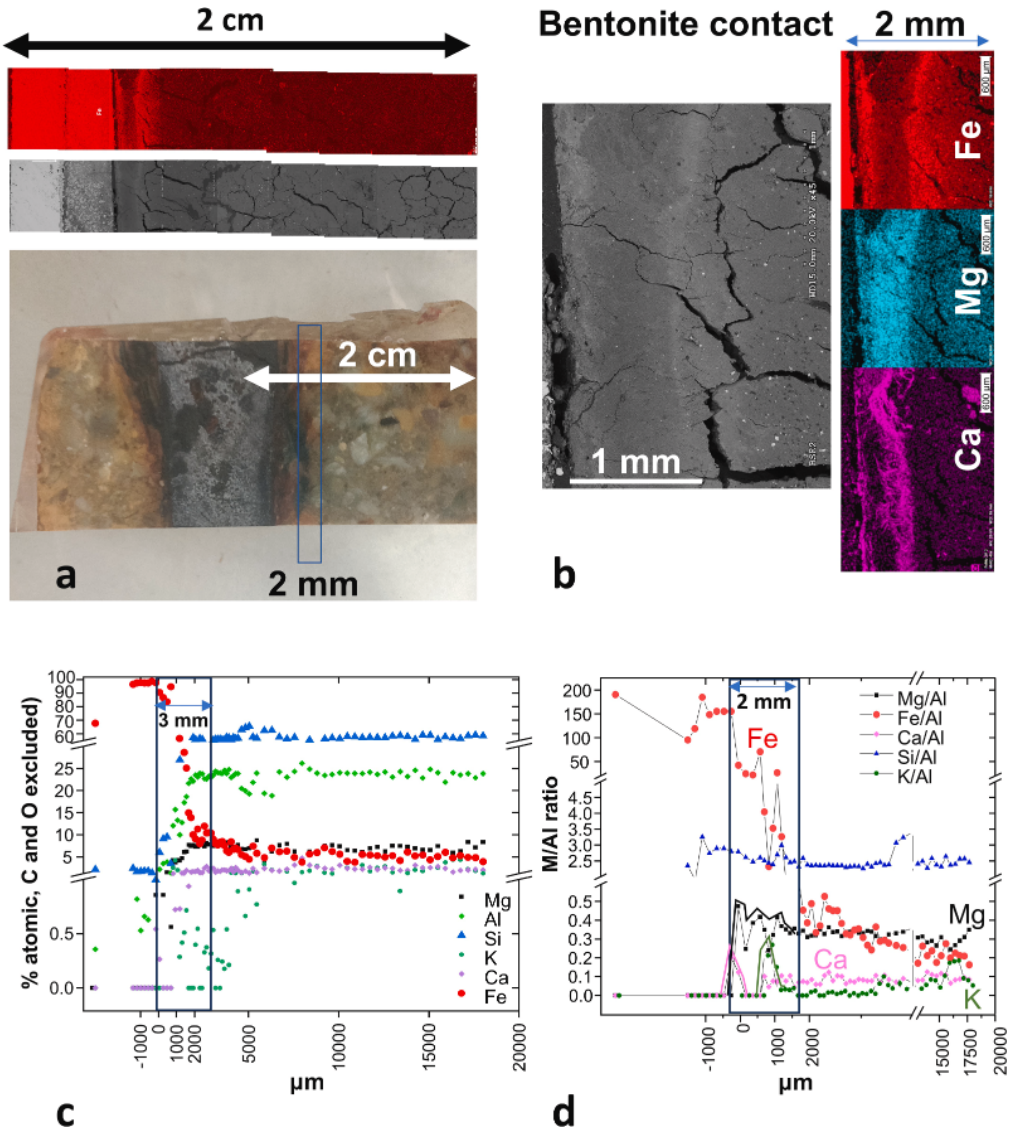

Fig. 6. Section 3 of the FeMo experiment. a. Cross section of the bentonite contact with iron powder showing the 2 mm EDX elemental mapping zone shown in detail in (b) and the 2 cm covering major elemental concentration profiles (% atomic excluding C and O) (c) and major elements normalized to Al (d).

tape used to fix the samples to the holder. Consequently, this zone is predominantly composed of iron oxide.

The bentonite at the contact (Fig. 9b) also shows high Fe content, and its smooth surfaces suggest the presence of iron oxide cements, making it impossible to calculate the structural formula needed to infer crystal-chemical aspects of the smectite, as highlighted in Fig. 8.

The iron oxides can be observed in detail, showing different morphologies precipitated in the polygonal voids left by dissolved metallic iron grains. Needle-like or dendritic aggregated grain morphologies are typical of Fe_2O_3 or FeOOH (respectively), originating from magnetite (with many examples in ore geology, e.g., [51]). Platy morphologies are also characteristic of hematite in these environments.

Needle-like and fine-grained morphologies (Fig. 9c and core precipitates in Fig. 9d) contain less C than the platy-tabular morphologies observed in Fig. 9d, suggesting the possible presence of siderite in this case.

Elemental maps have also been performed on an inner cross-section, perpendicular to the previous one, to assess the extent of iron diffusion and oxide precipitation in different (radial) orientations. The image in Fig. 10a shows the combination of backscattered electron images and elemental maps (SEM-BSE + EDX) measured from that radial configuration. The result confirms an extent of the Fe-diffusion affected zone clearly does exceed the first mm of the interface, although there are diffuse fringes of lower intensity with relatively low Fe contents.

These results seem to contradict the several millimetre-thick brown-orange staining visually observed in the bentonite, as the results above indicate that the alteration is limited to distances of less than one millimetre. A possible explanation for this discrepancy is that the dark brown halo was differentially spread at the upper and bottom flat contacts of the experiment due to the existence of preferential (flow) pathways. When a transverse cut is observed, separated from the surface contact zone with the experiment, Fe diffusion is very limited. Therefore, we consider the SEM-EDX elemental mapping results of this cross-section cut to be more accurate and representative of the spatial spread of the iron-stained halo.

3.4. Understanding of the hydrogeochemical processes and microstructural changes

Integrating micro-CT results, chemical gradients, mineralogy, and microstructure of the iron-bentonite interface in the FeMo long-term experiment enables us to determine the sequence of processes that

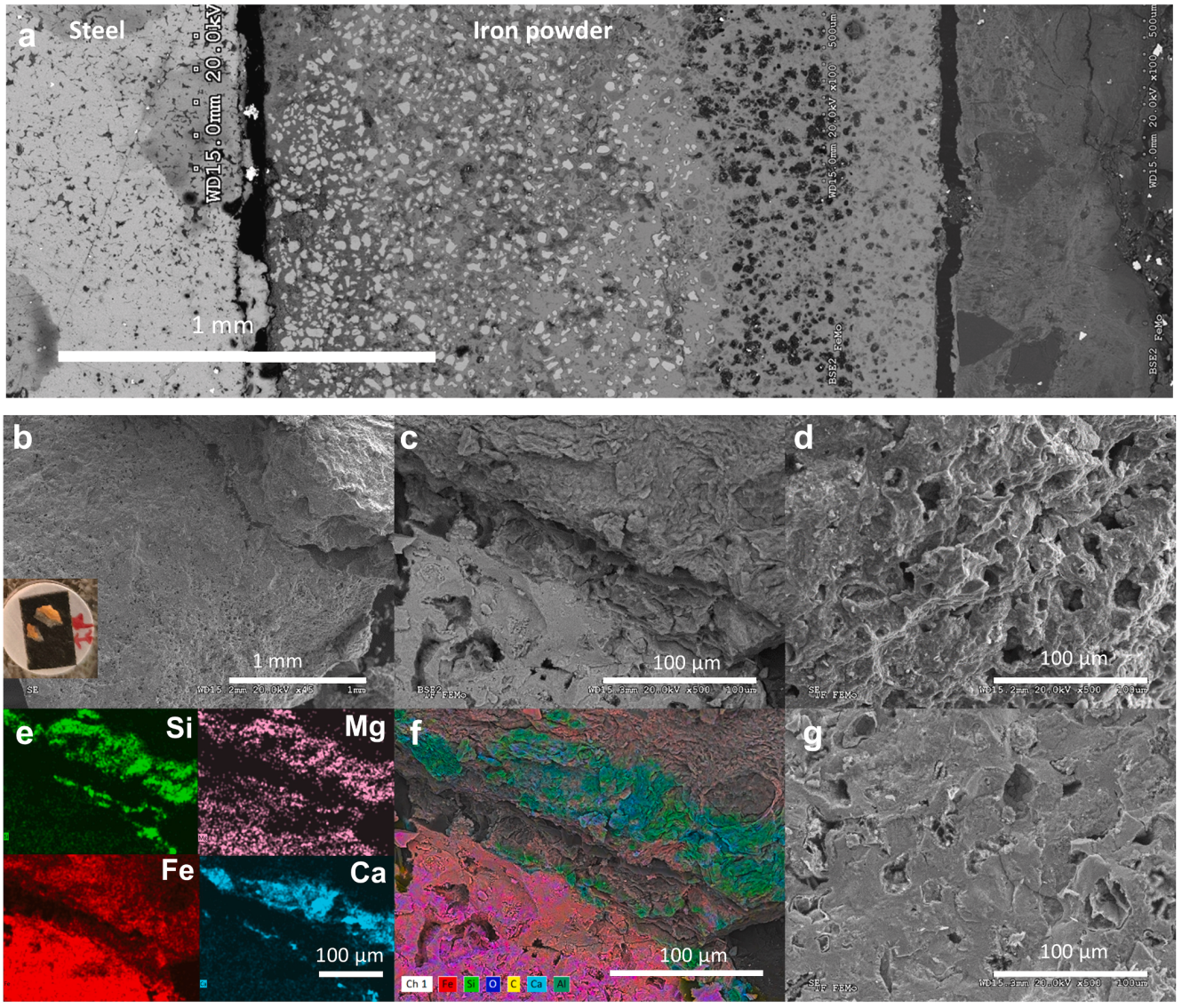

Fig. 7. a. Secondary electron (SE) SEM image of the porous altered iron layer; b. Detail of compact, layered, porous bentonite at the contact (BSE). c. Back scattered electrons (BSE) image detail of steel sinter, iron powder and bentonite. d. Elemental maps of Si (green), Mg (pink), Fe (red), and Ca (blue), corresponding to the "e" image. e. Detail of the iron zone (light grey) –bentonite contact (BSE image).

occurred during the 15 years of operation. The final alteration thicknesses of each material are also quantified, as well as the formation of microcracks, and the distance of iron penetration into the bentonite. Fig. 10b, c compiles graphically the results.

Iron powder exhibits a layered structure (Fig. 7a) with an inner layer of uncorroded iron, an intermediate layer of $Fe(OH)_2$ and Fe_3O_4, and an outer layer close to the bentonite mainly formed by FeOOH and $FeCO_3$. The experiment initiates with iron powder in contact with unsaturated bentonite and aerobic conditions due to the presence of atmospheric oxygen trapped during the assembly of the experimental set-up. During this first stage, corrosion occurs very rapidly by oxidation of the iron by the oxygen in the voids and pores ($Fe^0 \rightarrow Fe^{2+} + 2e^-$). Soon, the bentonite begins to hydrate with the granitic water that mixes with the pore water, which reacts with the Fe^{2+} to form ferrous hydroxide ($Fe^{2+} + H_2O \rightarrow Fe(OH)_2 + H_2$ (g)), which is relatively unstable in the presence of oxygen at low temperatures. Dissolution of Fe^{2+} in an aqueous phase and formation of hydrogen gas can result on the formation of the iron porous layer, about 250 µm thick, observed in Fig. 7a. At this point, dessiccation and microcracking may also occur due to the consumption of water in the corrosion process and the presence of the gas phase (Figs. 3 and 6) [13,18,19,46]. described this effect in their corrosion experiments of iron or carbon steel in contact to compacted bentonite or clay rock. The use of iron powder reduces the kinetic limitations of the corrosion process, so the amount of dissolved Fe^{2+} is higher in comparison with other geometries, such as foils or wires. Ferrous hydroxide can either evolve to magnetite via the Schikorr reaction ($3Fe(OH)_2 \rightarrow Fe_3O_4 + 2H_2O + H_2$(g)) [52] or can diffuse through the corrosion product layer and precipitate in the compacted bentonite block as oxides or oxyhydroxides filling the cracks and voids. The small diffusion coefficients of ferrous ions in compacted bentonite [12] favor stacking of corrosion products at the interface during first stages rather than migration into the bentonite, although with time diffusion occurs.

Once the system is oxygen depleted, precipitation of Fe(II)-phases starts. As hydration progresses carbonates are dissolved, which leads to deprotonation and finally, to the appearance of alkaline conditions in the vicinity of the Fe/bentonite interface. The absence of ferrihydrite and hematite indicates that the hydrolysis of Fe^{3+} occurred at alkaline pH.

Anaerobic corrosion of metallic iron results in the precipitation of Fe (II) hydroxide, which progressively converts to Fe(II, III) oxide

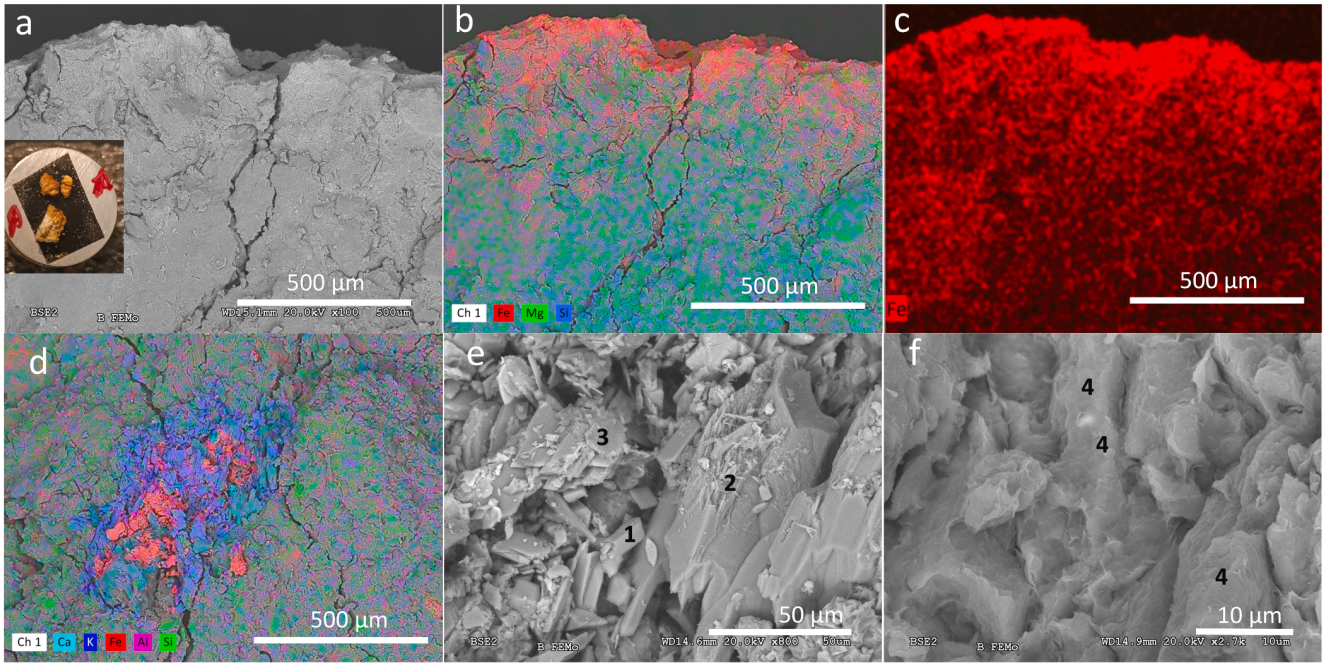

Fig. 8. Bentonite fragment detached from the iron powder interface. a. Photograph of bentonite sample in SEM holder; backscatter electron image (BSE), with iron staining at the top. b. Virtual coloured map outlining iron rim; c. Fe mapping rim; d. Detail of a K-Ca enrichment zone at 1 mm distance from the iron-stained interface; e. Crystal morphologies at Ca-K rich zone; euhedral K-feldspars and Ca-rich needles on plagioclase. f. Bentonite clay under the iron interface.

Table 4
Chemical composition of the specific zones analysed by SEM-EDX, expressed based on the adjusted mineral stoichiometry (silicates), in Fig. 8.

Sample	FeMo1	FeMo2		FeMo3	FeMo4		FEBEX	
Anion basis	O_8	O_8(3 s)	sd ±	$O_{10}(OH)_2$	$O_{10}(OH)_2$	sd ±	$O_{10}(OH)_2$	sd ±
Si(IV)	2.81	2.35	0.04	3.78	3.48	0.04	3.91	
Al(IV)	1.10	1.47	0.08	0.22	0.52	0.04	0.09	0.04
Fe(IV)	0.07	0.09	0.07					
sum tet	3.98	3.91						
Al(VI)				1.20	1.27	0.05	1.33	0
Mg(VI)				0.37	0.58	0.02	0.44	0
Fe(VI)				0.49	0.60	0.09	0.2	0
Ti(VI)				0.00	0.00			
sum oct				2.06	2.45	0.05	1.97	0
Na	0.00	0.72	0.03	0.13	0.18	0.03		
Ca	0.00	0.61	0.03	0.11	0.10	0.02	0.28	0.02
K	1.33	0.00	0.01	0.54	0.00		0.10	0.01
cat ch	1.33	1.94		0.90	0.38		1.97	0.02
mineral	Kfs	Pl		Mica	Sme d-t		Sme-d	

cat ch: cationic charge compensating isomorphic substitutions (i.e. Al^{4+} for Si^{4+} or Mg^{2+} for Al^{3+}); sum oct: sum of octahedral cations in phyllosilicates; Kfs: potassium feldspar; Pl: plagioclase; Sme: smectite; d: dioctahedral; t: trioctahedral. sd: standard deviation taken at least 3 samples.

(magnetite) (with production of gas), via the Schikorr reaction. If carbonates are present, themodynamically-stable siderite occurs, via chukanovite [47], which is a metastable phase.

Neoformation of silicates in the iron powder was not observed, and only evidence of the possible formation of tri-octahedral clay minerals, associated with the contact band with the bentonite. The concentration of Ca (presumably calcium carbonate at the contact) and Mg (serpentine-like or Fe-Mg saponite; [53]) suggest alkaline conditions at this interface and an important role of carbonates in the reaction. FEBEX bentonite has a relatively low SO_4 content (< 20 mmol/kg; [54]), which limits the potential precipitation of pyrite or pyrrhotite, frequently observed in these experiments in the presence of hydrogen [55].

3.5. Implications of the research

Long-term experiments are critical for understanding the long-lasting performance of engineered barriers in DGRs. In particular, this 15-year laboratory experiment represents a valuable source of empirical evidence on the evolution of iron-bentonite interactions under repository conditions. The extended duration of the experiment has made possible to observe slow, coupled geochemical processes, such as iron corrosion, mineral transformation, and redox changes that cannot be fully captured in short-term studies.

In DGR systems, corrosion of metal containers over time produces iron corrosion products that may interact with surrounding clay barriers. If container failure occurs and radionuclides with a high affinity for iron are released, their mobility will depend on these complex geochemical interactions. This experiment shows that, even after 15 years, the iron migration into bentonite remains limited and the barrier properties of the clay are preserved. Such findings significantly strengthen confidence in the long-term performance of engineered barriers, not only for the containment of radioactive waste, but also for other hazardous materials. In addition, by providing data over decadal timescales, the results support the calibration and validation of reactive

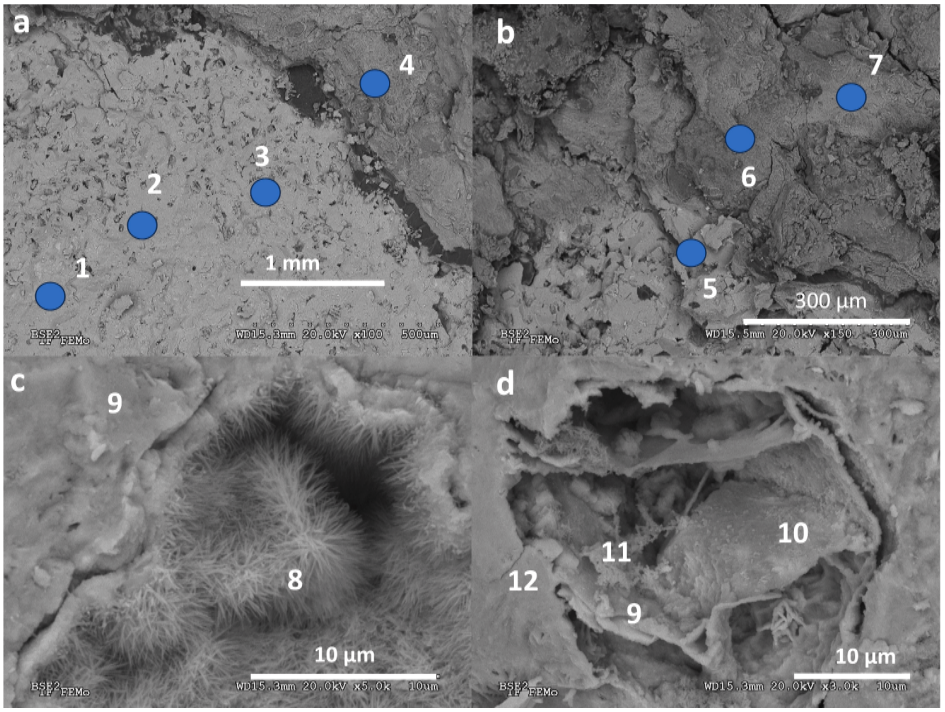

% atoms	1	2	3	4
C	10.9	12.7	12.6	16.6
O	57.9	57.5	55.5	59.7
Na				0.2
Mg				1.3
Al				3.0
Si				6.9
K				0.1
Ca				2.4
Fe	31.2	29.7	31.8	9.7

% atoms	5	6	7
C	9.8	28.3	13.0
O	59.6	52.2	65.8
Na		0.3	
Mg	0.2	0.5	0.1
Al		3.3	0.5
Si	0.3	6.6	1.6
K		0.8	
Ca	0.1	0.2	0.1
Fe	29.9	7.8	18.9

% atoms	8	9	10	11	12
C	14.7	12.1	15.6	15.7	14.9
O	64.3	60.8	55.2	57.5	51.6
Cr	0.1		0.1	0.1	0.5
Mn	0.1		0.1	0.1	0.4
Fe	20.5	27.7	29.0	26.6	32.4

Fig. 9. Chemical composition and detailed SEM aspects of the altered iron powder zone in contact with bentonite in the FeMo3 sample. a. Analysis of the iron oxide zone; b. Analysis of the bentonite contact; c. Needle-fibrous iron oxide precipitation in polygonal pores; d. Platy iron-rich precipitates in polygonal pores. All images are BSE.

transport and geochemical models, help constrain key parameters, and reduce uncertainties in long-term safety assessments. Ultimately, experiments of this kind are essential for building a robust scientific basis for the safety case of geological disposal systems.

However, there remains a need for higher-resolution characterization of Fe-binding sites on clay surfaces, and our understanding of structural rearrangements during adsorption or redox transformations is still limited, particularly under environmentally relevant conditions. Additionally, gas dissipation due to corrosion phenomena and the evolution of porosity, including clogging processes, pose significant challenges and are not yet fully understood.

The implications of this study extend beyond radioactive waste management. A mechanistic understanding of Fe-clay interactions, particularly their role in driving variations in physicochemical parameters such as redox conditions, is essential for advancing our knowledge of interfacial reactivity and transport phenomena in dynamic geochemical environments. This perspective contrast with the conventional approach of studying such systems under static conditions. In this context, insights gained from the experiment presented here can help the design of engineered surfaces, including Fe-oxide-coated materials or clay-based composites.

The in-depth analysis of barriers used for containing high-level radioactive waste is also relevant to other environmental challenges, such as those found in mining operations or landfills, since the underlying physical and chemical processes are largerly shared across different waste management contexts. Therefore, studying the migration of metals like iron is challenging because it poses a significant environmental problem, with the potential to contaminate soil and groundwater. In this sense, the zonation patterns of Fe, Mg, and Ca observed in this study may serve as a valuable tool for evaluating and optimising engineered barrier systems used in the containment of hazardous waste. By analyzing the distribution and concentration of these elements at the iron-bentonite interface, it becomes possible to assess barrier performance and identify areas for improvement. This approach enables the targeted adjustment of material composition and barrier design, ultimately enhancing the capacity to contain harmful substances and contributing to the overall safety and sustainability of modern waste management strategies.

4. Conclusions

Fe migration in compacted bentonite due to iron powder corrosion and Fe dissolution extends up to 3 mm. The presence of magnetite and siderite on the iron and bentonite sides of the interface indicates that the environment changed from oxidising to reducing conditions during the experiment, with alkaline conditions prevailing at the interface. As for the long-term value of this experiment, over 15 years, under water-saturated conditions and at room temperature, the mineralogical changes produced are limited to the millimeter scale.

The microstructure (µ-CT) and elemental mapping results obtained by SEM-EDX on sections perpendicular to the compacted iron powder cylinder are consistent with the formation of a band <5 mm thick in which iron-rich minerals have relatively concentrated. In fact, it is the first 3 mm that show iron contents higher than those of the original bentonite, and on a micrometric scale, if we consider the zone of concentration of corrosion products, corresponding to zones stained with black to brown iron oxides. These zones are locally propagated by fractures that extend further towards the contact surface with the flat cover, through which hydration has been maintained. However, µ-CT revealed the existence of a dense network of perpendicular fractures, which constitute the porosity detected by this technique. The morphology (SEM) and arrangement of porous features are then transferred to the bentonite contact and interpreted as the result of gas formation.

The formation of an irregular concentric oxide halo is evidence of diffusion of dissolved iron from the cylinder and perturbation of its transport by microcracks and preferential pathways. In general, the mobility of iron is very restricted to the first millimeter and the evolution with time is expected to be very limited. The gas dissipation needs to be studied further, as small mechanical disturbances are observed that can

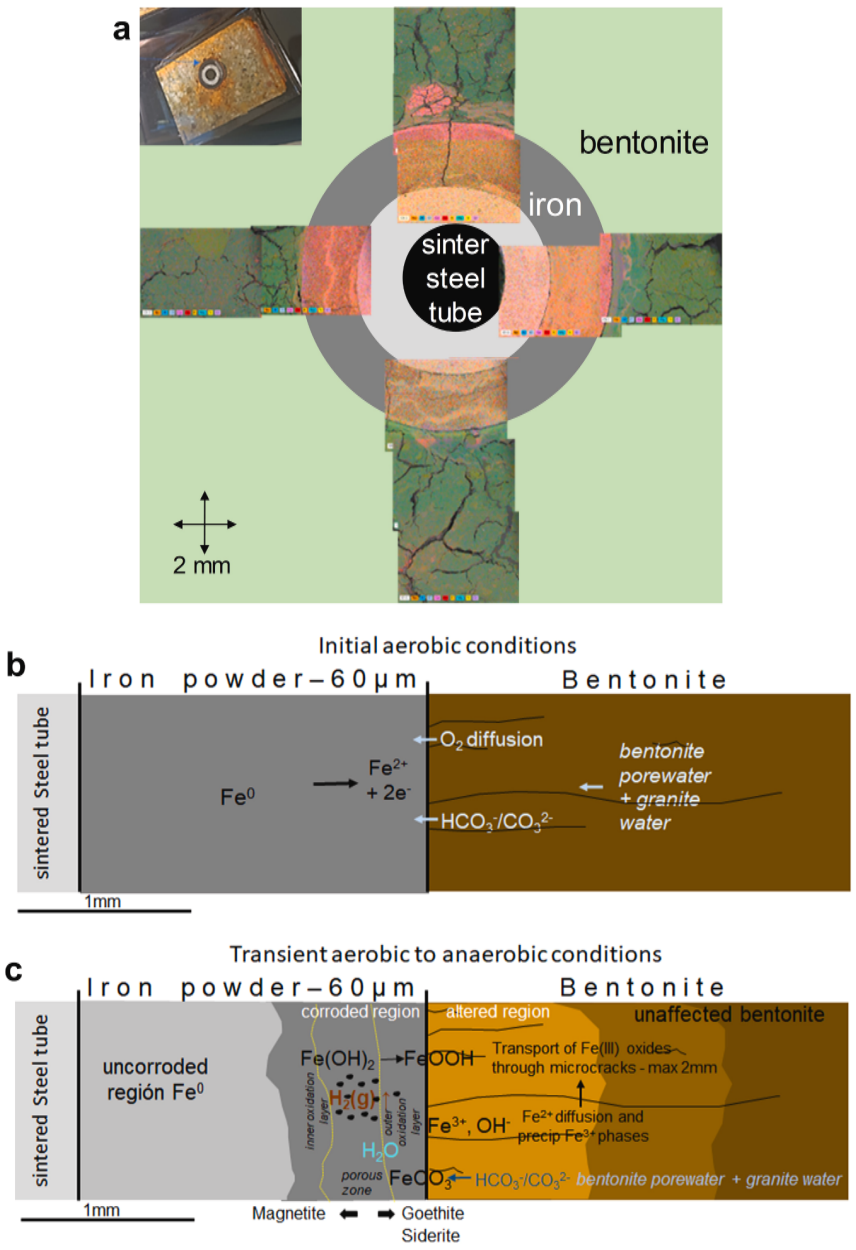

Fig. 10. a. Backscattered electron microscopy virtual colours image using EDX elemental maps of a transverse section made to capture the iron oxide halo around the iron powder ring disposed in FeMo experiment. b, c. Conceptual scheme of geochemical processes and its extension at the iron-bentonite interface with transient from oxic (b) to anoxic (c) conditions.

be attributed to gas generation, or at least to the formation of preferential pathways for iron diffusion in the bentonite.

Determining how migration occurs and which factors rule the mobilisation of heavy metals in containment barriers is essential. Multidisciplinary studies, as the one presented here, help determine the extent of migration and the conditions under which it occurs. This knowledge is crucial for developing waste management strategies that minimize metal migration or mitigate its consequences, ensuring compliance with environmental regulations.

CRediT authorship contribution statement

María J. Turrero: Writing – review & editing, Writing – original draft, Visualization, Supervision, Methodology, Investigation, Funding acquisition, Conceptualization. **Elena Torres:** Writing – review & editing, Validation, Methodology, Investigation, Conceptualization. **Pedro L. Martín:** Methodology, Conceptualization. **Raúl Fernandez:** Validation, Methodology, Investigation. **Ana I. Ruiz:** Investigation, Data curation. **Almudena Ortega:** Resources, Investigation. **Antonio Garralón:** Validation, Formal analysis, Data curation. **Belén Notario:** Writing – review & editing, Visualization, Methodology, Formal analysis. **Carlos Mota:** Visualization, Validation, Methodology. **Jaime F. Cuevas:** Writing – review & editing, Writing – original draft, Visualization, Supervision, Methodology, Investigation, Funding acquisition, Formal analysis.

Declaration of competing interest

The authors declare that they have no known competing financial interests or personal relationships that could have appeared to influence the work reported in this paper.

Acknowledgements

The experiment was designed and assembled in the context of the European NF-PRO project under grant number 516514 (https://cordis.europa.eu/project/id/2389), and was dismantled and analysed during the European EURAD-ACED project under grant number 847593 (https://www.ejp-eurad.eu/implementation/assessment-chemical-evolution-ilw-and-hlw-disposal-cells-aced). The authors thank the CENIEH, and especially Marina San Miguel Gutiérrez and Víctor Pérez Alonso, who collaborated in obtaining the micro-CT results.

Data availability

Data will be made available on request.

References

[1] R.W. Alexander, H.M. Reijonen, I.G. McKinley, Natural analogues: studies of geological processes relevant to radioactive waste disposal in deep geological repositories, Swiss J. Geosci. 108 (2015) 75–100, https://doi.org/10.1007/s00015-015-0187-y.

[2] Geological repository systems for safe disposal of spent nuclear fuels and radioactive waste, in: J. Apted, J. Ahn (Eds.), Woodhead Publishing Series in Energy, 2nd Edition, Elsevier, 2017, p. 802.

[3] K. Czurda, Clay Liners and Waste Disposal, chapter 11.3, in: F. Bergaya, B.K. G. Theng, G. Lagaly (Eds.), Developments in Clay Science, Vol. 1, Handbook of Clay Science, Elsevier, Amsterdam, The Netherlands, 2006, pp. 693–701, https://doi.org/10.1016/S1572-4352(05)01022-6.

[4] M.T. El-Saadony, A.M. Saad, N.A. El-Wafai, H.E. Abou-Aly, H.M. Salem, S. M. Soliman, T.A.A. El-Mageed, A.S. Elrys, S. Selim, M.E.A. El-Hack, S. Kappachery, K.A. El-Tarabily, S.F. AbuQamar, Hazardous wastes and management strategies of landfill leachates: a comprehensive review, Environ. Technol. Innov. 31 (2023) 103150, https://doi.org/10.1016/j.eti.2023.103150.

[5] F. King, Container materials for the storage and disposal of nuclear waste, Corrosion 69 (2013) 986–1011, https://doi.org/10.5006/0894.

[6] P. Sellin, O.X. Leupin, The use of clay as an engineered barrier in radioactive waste management - a review, Clay Clay Miner. 61 (2013) 477–498, https://doi.org/10.1346/CCMN.2013.0610601.

[7] J.W. Stucki, Properties and behaviour of iron in clay minerals, in: F. Bergaya, G. Lagaly (Eds.), Developments in Clay Science, Vol. 5, Handbook of Clay Science, Elsevier, Amsterdam, The Netherlands, 2013, pp. 559–611, https://doi.org/10.1016/B978-0-08-098258-8.00018-3.

[8] L. Charlet, C. Tournassat, Fe(II)-Na(I)-Ca(II) cation exchange on montmorillonite in chloride medium: evidence for preferential clay adsorption of chloride - metal ion pairs in seawater, Aquat. Geochem. 11 (2005) 115–137, https://doi.org/10.1007/s10498-004-1166-5.

[9] J. Wilson, G. Cressey, B. Cressey, J. Cuadros, K.V. Ragnarsdottir, D. Savage, M. Shibata, The effect of iron on montmorillonite stability. (II) Experimental investigation, Geochim. Cosmochim. Ac. 70 (2006) 323–336, https://doi.org/10.1016/j.gca.2005.09.023.

[10] J. Wilson, D. Savage, J. Cuadros, M. Shibata, K.V. Ragnarsdottir, The effect of iron on montmorillonite stability. (I) Background and thermodynamic considerations, Geochim. Cosmochim. Ac. 70 (2006) 306–322, https://doi.org/10.1016/j.gca.2005.10.003.

[11] M.L. Schlegel, C. Bataillon, C. Blanc, D. Prêt, E. Foy, Anodic activation of iron corrosion in clay media under water saturated conditions at 90 °C: characterization of the corrosion interface, Environ. Sci. Technol. 44 (2010) 1503, https://doi.org/10.1021/es9021987.

[12] K. Idemitsu, S. Yano, X. Xia, Y. Inagaki, T. Arima, T. Mitsugashira, M. Hara, Y. Suzuki, Diffusion behavior of iron corrosion products in buffer materials, Mater. Res. Soc. Symp. Proc. 713 (2002) 113–120, https://doi.org/10.1557/PROC-713-JJ11.9.

[13] X. Xia, K. Idemitsu, T. Arima, Y. Inagaki, T. Ishidera, S. Kurosawa, K. Iijima, H. Sato, Corrosion of carbon steel in compacted bentonite and its effect on neptunium diffusion under reducing condition, Appl. Clay Sci. 28 (2005) 89100, https://doi.org/10.1016/j.clay.2004.01.002.

[14] L. Carlson, O. Karnland, V.M. Oversby, A. Rance, N. Smart, M. Snellman, M. Vähänen, L.O. Werme, Experimental studies of the interactions between anaerobically corroding iron and bentonite, Phys. Chem. Earth 32 (2007) 334–345, https://doi.org/10.1016/j.pce.2005.12.009.

[15] L. Johnson, F. King, The effect of the evolution of environmental conditions on the corrosion evolutionary path in a repository for spent fuel and high-level waste in Opalinus Clay, J. Nucl. Mater. 379 (2008) 9–15, https://doi.org/10.1016/j.jnucmat.2008.06.003.

[16] F. King, D.S. Hall, P.G. Keech, Nature of the near-field environment in a deep geological repository and the implications for the corrosion behaviour of the container, Corros. Eng. Sci. Tech. 52 (2017) 25–30, https://doi.org/10.1080/1478422X.2017.1330736.

[17] K. Idemitsu, S.A. Nessa, S. Yamazaki, H. Ikeuchi, Y. Inagaki, T. Arima, Migration behaviour of ferrous ion in compacted bentonite under reducing conditions controlled with potentiostat, Mater. Res. Soc. Symp. Proc. 1107 (2008) 501–508, https://doi.org/10.1557/proc-1107-501.

[18] N. Smart, B. Reddy, A.P. Rance, D.J. Nixon, N. Diomidis, The anaerobic corrosion of carbon steel in saturated compacted bentonite in the Swiss repository concept, Corros. Eng. Sci. Techn. 52 (2017) 113–126, https://doi.org/10.1080/1478422X.2017.1316088.

[19] O. Leupin, N.R. Smart, Z. Zhang, M. Stefanoni, U. Angst, A. Papafotiou, N. Diomidis, Anaerobic corrosion of carbon steel in bentonite: an evolving interface, Corros. Sci. 187 (2021) 109523, https://doi.org/10.1016/j.corsci.2021.109523.

[20] K.G. Bhattacharyya, S.S. Gupta, Kaolinite and montmorillonite as adsorbents for Fe (III), Co(II) and Ni(II) in aqueous medium, Appl. Clay Sci. 41 (2008) 1–9, https://doi.org/10.1016/j.clay.2007.09.005.

[21] T. Gebrenegus, T.A. Ghezzehei, M. Tuller, Physicochemical controls on initiation and evolution of desiccation cracks in sand–bentonite mixtures: x-ray CT imaging and stochastic modelling, J. Contam. Hydrol. 126 (2011) 100–112, https://doi.org/10.1016/j.jconhyd.2011.07.004.

[22] S. Tomioka, T. Kozaki, H. Takamatsu, N. Noda, S. Nisiyama, N. Kozai, S. Suzuki, S. Sato, Analysis of microstructural images of dry and water-saturated compacted bentonite samples observed with X-ray micro CT, Appl. Clay Sci. 47 (2010) 65–71, https://doi.org/10.1016/j.clay.2008.09.001.

[23] T. Harjupatana, J. Alaraudanjoki, M. Kataja, X-ray tomographic method for measuring three-dimensional deformation and water content distribution in swelling clays, Appl. Clay Sci. 114 (2015) 386–394, https://doi.org/10.1051/e3sconf/20160918005.

[24] T. Kozaki, S. Suzuki, N. Kozai, S. Sato, H. Ohashi, Observation of microstructures of compacted bentonite by Microfocus X-ray computerized tomography (Micro-CT), J. Nucl. Sci. Techn. 38 (2001) 697–699, https://doi.org/10.1080/18811248.2001.9715085.

[25] C. Kawaragi, T. Yoneda, T. Sato, K. Kaneko, Microstructure of saturated bentonites characterized by X-ray CT observations, Eng. Geol. 106 (2009) 51–57, https://doi.org/10.1016/j.enggeo.2009.02.013.

[26] L. Luo, H. Lin, P. Halleck, Quantifying soil structure and preferential flow in intact soil using X-ray computed tomography, Soil Sci. Soc. Am. J. 72 (2008) 1058–1069, https://doi.org/10.2136/sssaj2007.0179.

[27] K.M. Grayling, S.D. Young, C.J. Roberts, M.I. de Heer, I.M. Shirley, C.J. Sturrock, S. J. Mooney, The application of X-ray micro computed tomography imaging for tracing particle movement in soil, Geoderma 321 (2018) 8–14, https://doi.org/10.1016/j.geoderma.2018.01.038.

[28] C. Wittebroodt, M.J. Turrero, E. Torres, P. Gómez, A. Garralón, B. Notario, M. Sanmiguel, J. Cuevas, C. Mota, A.I. Ruiz, R. Fernández, A. Ortega, J. Samper, A. Mon, L. Montenegro, J. Hadi, M. Kizcka, A. Jenni, J. Goethals, J.M. Greneche, K. David, P. Wersin, V. Havlová, A.M. Miranda Norma, M. Klajmon, D. Dobrev, P. Večerník, M. Fabian, D. Jacques, Final technical report on the steel/clay material interactions. Final Version of Deliverable D2.7 of the HORIZON 2020 Project EURAD. EC Grant agreement no: 847593, 2024.

[29] Enresa, 1998. FEBEX project: bentonite: origin, properties and fabrication of the blocks, Publicación Técnica ENRESA 05/98, Enresa, Madrid, 170 pp.

[30] A. Garralón, P. Gómez, M.J. Turrero, E. Torres, B. Buil, L. Sánchez, J. Peña, Hydrogeochemical characterisation of the groundwater in the FEBEX gallery. NAGRA Arbeitsbericht NAB 16-14, 2017, p. 125. URL, http://www.grimsel.com/gts-phase-vi/febex-dp/febex-dp-literature-publications.

[31] Dragonfly 3D World by Object Research Systems (ORS). Comet Technologies Canada Inc. https://www.theobjects.com/dragonfly, version 2022.2.

[32] J. Schindelin, I. Arganda-Carreras, E. Frise, V. Kaynig, M. Longair, T. Pietzsch, S. Preibisch, C. Rueden, S. Saalfeld, B. Schmid, J.-Y. Tinevez, D.J. White, V. Hartenstein, K. Eliceiri, P. Tomancak, A. Cardona, Fiji: an open-source platform for biological-image analysis, Nat. Methods 7 (2012) 676–682, https://doi.org/10.1038/nmeth.2019.

[33] L.P. Meier, G. Kahr, Determination of the cation exchange capacity (CEC) of clay minerals using the complexes of copper(II) ion with triethylenetetramine and tetraethylenepentamine, Clay. Clay Miner. 47 (1999) 386–388, https://doi.org/10.1346/CCMN.1999.0470315.

[34] B.L. Sawhney, Potassium and cesium ion selectivity in relation to clay mineral microstructure, Clay. Clay Miner. 18 (1970) 47–52, https://doi.org/10.1346/CCMN.1970.0180106.

[35] N.H. Aguilera, M.L. Jackson, Iron oxide removal from soils and clays, Soil Sci. Soc. Am. J. 17 (1953) 359–364, https://doi.org/10.2136/sssaj1953.03615995001700040015x.

[36] O.P. Mehra, M.L. Jackson, Iron oxide removal from soils and clays by a dithionite-citrate system buffered with sodium bicarbonate, Clay. Clay Miner. 7 (1958) 317–327, https://doi.org/10.1346/CCMN.1958.0070122.

[37] J. Xiao, Y. Song, Y. Li, Comparison of quantitative X-ray diffraction mineral analysis methods, Minerals 13 (2023) 566, https://doi.org/10.3390/min13040566.

[38] P. Zhao, L. Lu, X. Liu, A.G. De la Torre, X. Cheng, Error analysis and correction for quantitative phase analysis based on Rietveld-internal standard method: whether the Minor phases can Be ignored? Crystals 8 (2018) 110, https://doi.org/10.3390/cryst8030110.

[39] F. Larachi, R. Hannaoui, P. Horgue, F. Augier, Y. Haroun, S. Youssef, E. Rosemberg, M. Prat, M. Quintard, X-ray microtomography and pore network modeling of single-phase fixed-bed reactors, Chem. Eng J. 240 (2014) 290–306, https://doi.org/10.1016/j.cej.2013.11.077.

[40] M. Doube, M.M. Kłosowski, I. Arganda-Carreras, F. Cordelières, R.P. Dougherty, J. Jackson, B. Schmid, J.R. Hutchinson, S.J. Shefelbine, BoneJ: free and extensible

bone image analysis in image, Bone 47 (2010) 1076–1079, https://doi.org/10.1016/j.bone.2010.08.023.
[41] L.J. Munkholm, R.J. Heck, B. Deen, Soil pore characteristics assessed from X-ray micro-CT derived images and correlations to soil friability, Geoderma 181–182 (2012) 22–29, https://doi.org/10.1016/j.geoderma.2012.02.024.
[42] M.V. Villar, R. Gómez-Espina, R. Campos, I. Barrios, L. Gutiérrez, Porosity changes due to hydration of compacted bentonite, in: C. Mancuso, C. Jommi, F. D'Onza (Eds.), Unsaturated Soils: Research and Applications Vol. 1, Springer, Berlin, Heidelberg, 2012, pp. 137–144, https://doi.org/10.1007/978-3-642-31116-1_18.
[43] Y. Meng, Q. Wang, W. Su, W. Ye, Y. Chen, Experimental evidence on the cracking and sealing mechanisms of compacted bentonite by using microfocus X-ray computed tomography, Eng. Geol. 322 (2023) 107153, https://doi.org/10.2139/ssrn.4313544.
[44] M. Zaidi, N. Mokni, M. Dymitrowska, K. Liu, Analyzing structural changes induced by gas migration in heterogeneous pellet/powder bentonite mixtures through X-ray computed micro-tomography, J. Rock Mech. Geotech. Eng. 17 (2024) 3198–3212, https://doi.org/10.1016/j.jrmge.2024.09.054.
[45] Y. Zhang, Q. Zheng, J. Zhou, H. Ren, H. Chen, Characterization of fresh and corroded nano zero-valent iron (nZVI) to remove Cr(VI) in soil environment, Environ. Monit. Assess. 197 (2025) 620, https://doi.org/10.1007/s10661-025-14093-4.
[46] R. Mosser-Ruck, J. Sterpenich, N. Michau, M.-C. Jodin-Caumon, A. Randi, M. Abdelmoula, O. Barres, M. Cathelineau, Serpentinization and H_2 production during an iron-clay interaction experiment at 90C under low CO_2 pressure, Appl. Clay Sci. 191 (2020) 105609, https://doi.org/10.1016/j.clay.2020.105609.
[47] I. Azoulay, C. Rémazeilles, P. Refait, Determination of standard gibbs free energy of formation of chukanovite and Pourbaix diagrams of iron in carbonated media, Corros. Sci. 58 (2012) 229–236, https://doi.org/10.1016/j.corsci.2012.01.033.
[48] M.J. Russell, A.J. Hall, The onset and early evolution of life, Geol. Soc. Am. Mem. 198 (2006) 1–32, https://doi.org/10.1130/2006.1198(01).
[49] J. Cuevas, M.Á. Cabrera, C. Fernández, C. Mota-Heredia, R. Fernández, E. Torres, M.J. Turrero, A.I. Ruiz, Bentonite powder XRD quantitative analysis using Rietveld refinement: revisiting and updating bulk semiquantitative mineralogical compositions, Minerals 12 (2022) 772, https://doi.org/10.3390/min12060772.
[50] S.W. Bailey, Structures of layer silicates, in: G.W. Brindley, G. Brown (Eds.), Crystal Structures of Clay Minerals and Their X-Ray Identification, Mineralogical Society Monograph No. 5, 1984, pp. 1–124. London.
[51] R.C. Morris, Microplaty hematite—Its varied nature and genesis, Aust. J. Earth Sci. 59 (2012) 411–434, https://doi.org/10.1080/08120099.2011.626453.
[52] R.M. Cornell, U. Schwertmann, The Iron Oxides. Structure, Properties, Reactions, Occurences and Uses, 2nd Edition, WILEY-VCH Verlag GmbH & Co. KGaA, Weinheim, 2003, p. 664.
[53] M.C. Cheshire, F.A. Caporuscio, C.J. Colón, K.E. Norskog, Fe-saponite growth on low-carbon and stainless steel in hydrothermal-bentonite experiments, J. Nucl. Mat. 511 (2018) 353–366, https://doi.org/10.1016/j.jnucmat.2018.09.038.
[54] J. Cuevas, M.V. Villar, P.L. Martín, J. Cobeña, S. Leguey, Thermo-hydraulic gradients on bentonite: distribution of soluble salts, microstructure and modification of the hydraulic and mechanical behavior, Appl. Clay Sci. 22 (2002) 25–38, https://doi.org/10.1016/S0169-1317(02)00109-6.
[55] M. Didier, L. Leone, J.M. Greneche, E. Giffaut, L. Charlet, Adsorption of hydrogen gas and redox processes in clays, Environ. Sci. Technol. 46 (2012) 3574–3579, https://doi.org/10.1021/es204583h.